Chakrabarti et al. Nanoscale Research Letters (2016) 11:389
DOI 10.1186/s11671-016-1602-7

Nanoscale Research Letters

NANO EXPRESS Open Access

Temperature-Dependent Non-linear Resistive Switching Characteristics and Mechanism Using a New W/WO_3/WO_x/W Structure

Somsubhra Chakrabarti[1], Subhranu Samanta[1], Siddheswar Maikap[1*], Sheikh Ziaur Rahaman[1,2] and Hsin-Ming Cheng[3]

Abstract

Post-metal annealing temperature-dependent forming-free resistive switching memory characteristics, Fowler-Nordheim (F-N) tunneling at low resistance state, and after reset using a new W/WO_3/WO_x/W structure have been investigated for the first time. Transmission electron microscope image shows a polycrystalline WO_3/WO_x layer in a device with a size of 150 × 150 nm^2. The composition of WO_3/WO_x is confirmed by X-ray photo-electron spectroscopy. Non-linear bipolar resistive switching characteristics have been simulated using space-charge limited current (SCLC) conduction at low voltage, F-N tunneling at higher voltage regions, and hopping conduction during reset, which is well fitted with experimental current-voltage characteristics. The barrier height at the WO_x/W interface for the devices annealed at 500 °C is lower than those of the as-deposited and annealed at 400 °C (0.63 vs. 1.03 eV). An oxygen-vacant conducting filament with a diameter of ~34 nm is formed/ruptured into the WO_3/WO_x bilayer owing to oxygen ion migration under external bias as well as barrier height changes for high-resistance to low-resistance states. In addition, the switching mechanism including the easy method has been explored through the current-voltage simulation. The devices annealed at 500 °C have a lower operation voltage, lower barrier height, and higher non-linearity factor, which are beneficial for selector-less crossbar memory arrays.

Keywords: WO_3 switching material, Temperature, F-N tunneling, Barrier height, Simulation

Background

Recently, resistive random access memory (RRAM) has become a promising candidate to replace three-dimensional FLASH for crossbar applications at a low cost owing to its simple structure, low power consumption, and high-speed operation [1–4]. Although different switching materials such as Ta_2O_5 [5–7], HfO_2 [8, 9], TiO_2 [10–12], and Al_2O_3 [13–15] have been reported, however, only a few studies have been reported on WO_3 material [16, 17]. WO_3 has an acceptable energy gap of 3.25 eV [18] and Gibbs free energy of approximately −529 kJ/mol at 300 K [19]. Chien et al. [16] reported that the Frenkel effect modified the space-charge limited current (SCLC) in a W/WO_x/TiN structure. Biju et al. [17] reported Schottky emission in low field and Poole-Frankel in high field in a Pt/WO_3/W structure. Although different structures have been reported to amplify the RRAM characteristics, its temperature-dependent non-linear switching characteristics and mechanism are still unclear [20]. In this regard, the current transport mechanism is one of the key factors in understanding the resistive switching behavior. Many authors have proposed different structures in the current conduction mechanism [21–23]. The barrier height in between the switching material and the electrode can control the interfacial-type bipolar characteristics [5, 21]. On the other hand, non-linear resistive switching characteristics are useful for reducing the sneak path in crossbar architecture, which can be solved using a complementary structure [7, 24] or selector [25]. If the RRAM device shows non-linearity without a selector, then

* Correspondence: sidhu@mail.cgu.edu.tw
[1]Thin Film Nano Tech. Lab., Department of Electronic Engineering, Chang Gung University, 259 Wen-Hwa 1st Rd., Kwei-Shan, Tao-Yuan 333, Taiwan
Full list of author information is available at the end of the article

Springer Open

© 2016 The Author(s). **Open Access** This article is distributed under the terms of the Creative Commons Attribution 4.0 International License (http://creativecommons.org/licenses/by/4.0/), which permits unrestricted use, distribution, and reproduction in any medium, provided you give appropriate credit to the original author(s) and the source, provide a link to the Creative Commons license, and indicate if changes were made.

the above issue can be solved in an easy way. Although many structures with different transport mechanism have been reported, a simple $W/WO_3/WO_x/W$ RRAM device in the same material has not been reported yet. Nonlinear forming-free bipolar resistive switching characteristics using a simple $W/WO_3/WO_x/W$ structure are observed for as-deposited, 400 °C, and 500 °C annealed devices. A polycrystalline WO_3/WO_x layer is confirmed by both high-resolution transmission electron microscope (HRTEM) images and X-ray photo-electron spectroscope (XPS) spectra. Temperature-dependent SCLC characteristics at low voltage and Fowler-Nordheim (F-N) tunneling at high voltage for both low-resistance state (LRS) and high-resistance state (HRS) are observed, even after reset. The switching mechanism is explained by oxygen-vacant conducting filament (CF) formation/rupture into the WO_3/WO_x bilayer, and a new method of current-voltage (I-V) simulation is explored. Compared to other memory devices, the devices annealed at 500 °C have higher non-linearity factor, lower operation voltage, and lower barrier heights.

Methods

First, a Si wafer was cleaned by the standard Radio Corporation of America (RCA) process. Then, a 200-nm-thick SiO_2 was grown by a thermal oxidation method. A 200-nm-thick tungsten (W) as a bottom electrode (BE) was deposited on the SiO_2/Si substrate. Then, a SiO_2 layer with a thickness of approximately 150 nm was deposited by physical vapor deposition method for via-hole patterns. A small via hole with a size of 150×150 nm^2 was formed by a standard photo-lithography process. Then, the WO_3 layer was deposited by rf sputtering. After that, a WO_x layer was deposited, and lastly, W top electrode (TE) was deposited using the same rf sputtering system. The pressure of the sputtering chamber was kept at 10 mTorr during deposition, and the deposition power was 100 W. The flow rate of argon (Ar) gas was 25 sccm during deposition of W TE. By controlling the oxygen (O_2) flow rate with Ar flow, the WO_3 layer with a thickness of 4 nm on the BE and the WO_x layer with a thickness of 5 nm on the WO_3 layer were deposited. For the WO_3 layer, 70 % oxygen is used whereas 30 % oxygen is used for the WO_x layer. Finally, a lift-off process was performed to obtain the RRAM devices. These devices were post-metal annealed (PMA) at 400 °C (S2) and 500 °C (S3) for 10 min in ambient N_2. These annealed devices were compared with the as-deposited one (S1). A schematic view of a RRAM device is shown in Fig. 1a. Memory characteristics were measured by an Agilent 4156C semiconductor parameter analyzer.

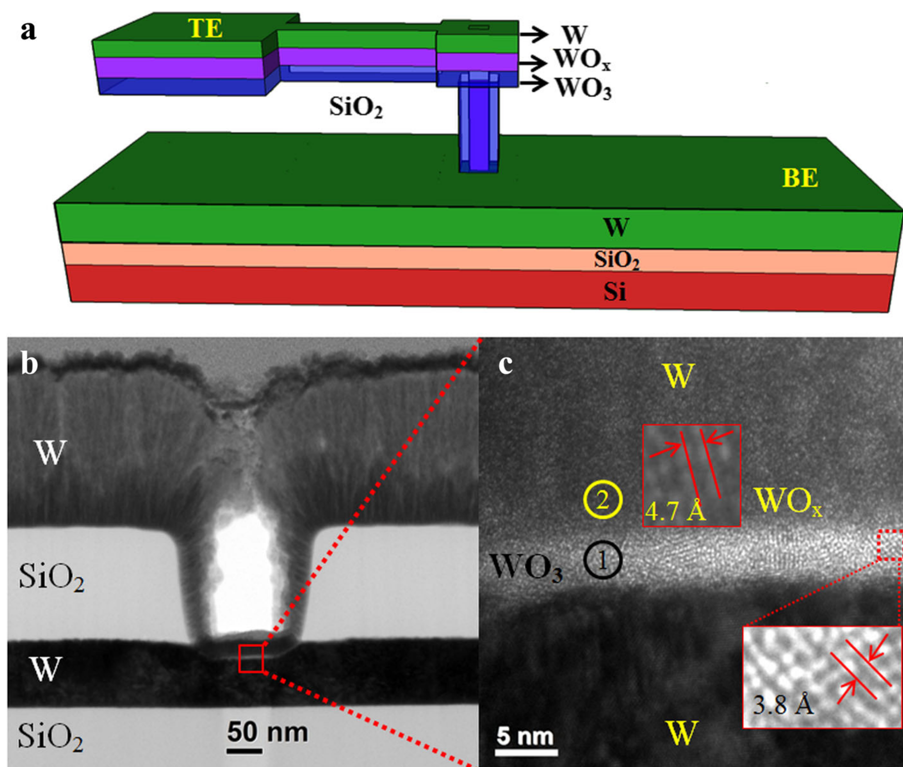

Fig. 1 **a** Schematic view of a $W/WO_3/WO_x/W$ resistive switching memory device. **b** TEM image shows 150×150 nm^2 devices. **c** HRTEM image confirms the WO_3/WO_x layer. The crystalline WO_3 and WO_x layers with d-spacing are shown inset

The sweep voltage was applied on the TE, whereas the BE was grounded during the measurement.

Results and Discussion

Figure 1b shows a TEM image of a RRAM device with a via-hole size of 150×150 nm^2. A WO_3 switching layer of S1 device with a thickness of an approximately 4-nm layer is shown on the W BE (Fig. 1c). The oxygen-deficient layer, i.e., WO_x, with a thickness of approximately 5 nm was deposited. Due to the similar material of the WO_x/W TE, an interface was not observed. The WO_3/WO_x layer was polycrystalline. The polycrystalline grain size will be increased with annealing temperature. Ottaviano et al. [26] reported that the crystallite size of 5-nm-thick WO_3 changes from 26 to 35 nm due to annealing from 350 to 500 °C. The polycrystalline WO_3 layer had a d-spacing value of 3.8 Å, which was similar to the reported value of 3.835 Å for the (002) WO_3 layer [27]. The measured value of d-spacing of WO_x was 4.7 Å, which was the same to the reported value of WO_x (4.7 Å, [28]). The presence of the WO_3 and WO_x layers was also confirmed by XPS analysis (Fig. 2). Two positions marked (1) and (2) were leveled on the HRTEM image in Fig. 1c, which were obtained from the XPS depth profile of the W TE/WO_x/WO_3/W BE sample. By etching layer by layer from the sample surface, the XP spectra were measured. The binding energy peaks centered at 31.6 and 33.8 eV corresponded to the W $f_{7/2}$ and W $f_{5/2}$, respectively, whereas the peaks centered at 35.9 and 38.1 eV corresponded to the WO_3 $f_{7/2}$ and WO_3 $f_{5/2}$ core-level electrons, respectively. Those peaks were also confirmed by Kawasaki et al. [29]. It was observed that the WO_3 intensity at the marked region (1) was stronger than that of the peak at the marked region (2). The atomic percentages of WO_3 and W were found to be 57.33 and 42.66 % at the marked region (1), respectively, whereas those values were 23.52 and 76.43 % at the marked region (2), respectively. Therefore, marked region (1) was an oxygen-rich layer, i.e., the WO_3 layer, whereas marked region (2) was an oxygen-deficient layer, i.e., the WO_x layer. The resistive switching characteristics of WO_3/WO_x bilayer have been explained below.

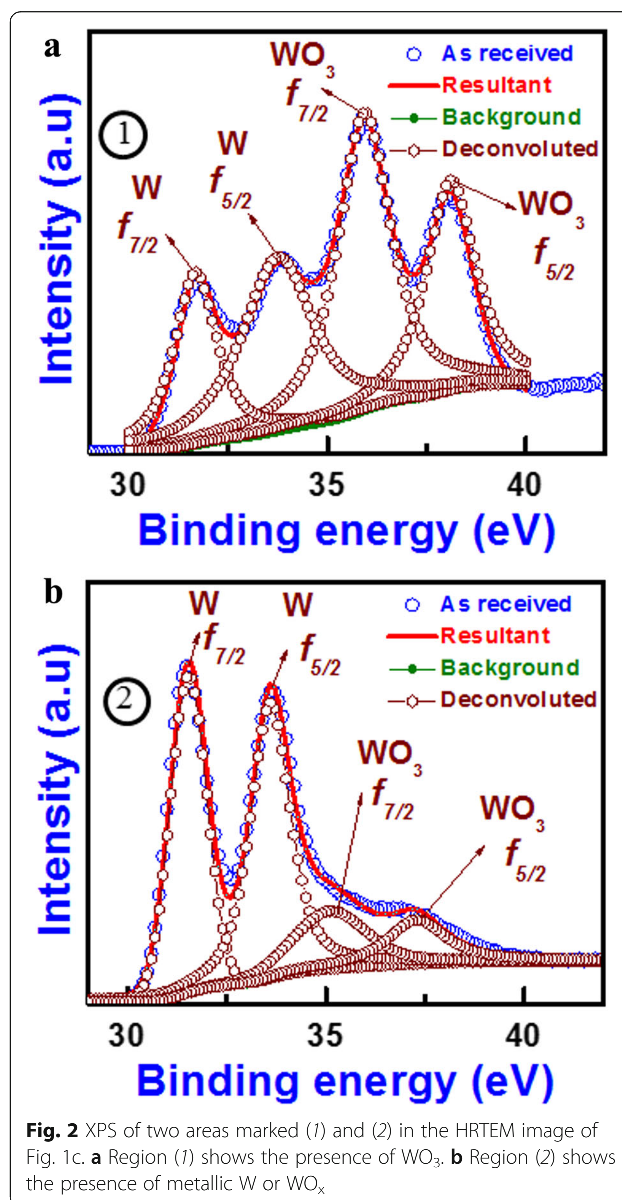

Fig. 2 XPS of two areas marked (*1*) and (*2*) in the HRTEM image of Fig. 1c. **a** Region (*1*) shows the presence of WO_3. **b** Region (*2*) shows the presence of metallic W or WO_x

Figure 3 shows the I-V characteristics of the S1, S2, and S3 devices under a current compliance (CC) of 500 μA. The voltages of the S1, S2, and S3 devices were set at 4.5, 5.5, and 3.6 V, respectively, and the reset voltages were −2.5, −2.9, and −2.35 V, respectively. These devices were forming free, i.e., the first cycle (on pristine device) is almost similar to the next cycles [30]. During set, the oxygen ions were migrated from the WO_3 layer by breaking W-O bonds to the WO_x/W interface and the oxygen-vacancy CF is formed. The device reached to LRS. During reset, oxygen ions were migrated from the WO_x/W interface to the WO_3 layer as well as the CF is oxidized and the device reached to HRS. The SCLC [31] was observed at the low bias regions for all the devices.

$$J = \frac{9\epsilon_r \varepsilon_0 \mu V^2}{8L^3} \tag{1}$$

where J is the current density, ε_r is the relative permittivity of the insulating material, ε_0 (8.85×10^{-12} F/m) is the permittivity of free space, μ is the electron mobility, and L is the thickness of the switching layer. From the above equation, I-V curves in both positive (+ve) and negative (−ve) bias regions were plotted in ln(I) vs. ln(V) scale (Fig. 4). The SCLC fittings consist of an ohmic region ($I \ \alpha \ V$) with slope values from 1.05 to 1.3 and Child's

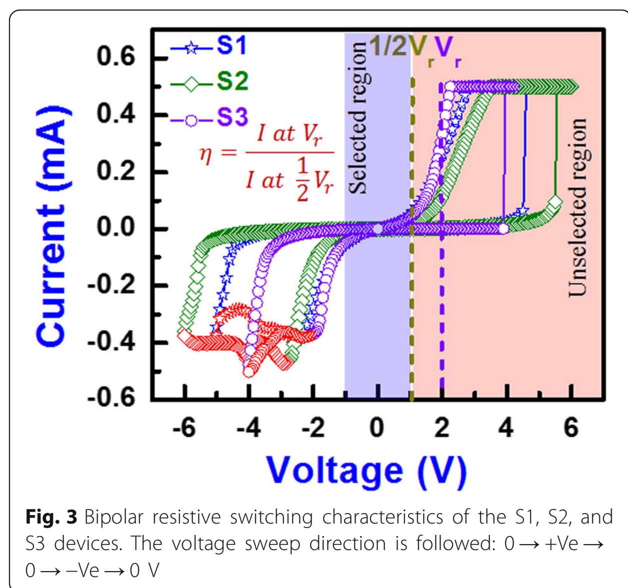

Fig. 3 Bipolar resistive switching characteristics of the S1, S2, and S3 devices. The voltage sweep direction is followed: 0 → +Ve → 0 → −Ve → 0 V

law region ($I \alpha V^2$) with slope values from 1.9 to 2.17 for both HRS and LRS. The slope value of the S1 devices is slightly higher (1.3) than unity, but the S2 and S3 devices have close to unity. The reason behind this is the number of defects was decreased after port-metal annealing treatment. Therefore, the S1 devices followed the trap-charge controlled (TC) SCLC whereas the S2 and S3 devices followed SCLC at low bias regions in both HRS and LRS. At the higher bias region of the HRS and LRS, the F-N tunneling equation [31, 32] is below:

$$J = \frac{q^3 E^2}{8\pi h q \phi_B} \exp\left\{-\frac{8\pi (2qm^*)^{\frac{1}{2}}}{3hE}\phi_B^{\frac{3}{2}}\right\} \quad (2)$$

where h (6.62×10^{-34} J s) is Plank's constant, q is electronic charge (1.6×10^{-19} C), m^* is the effective electron mass, and E is the electric field. From F-N tunneling, $\ln(J/E^2)$ was plotted as a function of $1/E$. Figure 5a, b shows the F-N tunneling fitting at the +ve and −ve regions for both HRS and LRS. The critical electric field (E_c) values at HRS for set were 3.03, 3.57, and 2.7 MV cm^{-1} and those values after reset were 3.7, 5, and 3.5 MV cm^{-1} for the S1, S2, and S3 devices, respectively. It is interesting to note that the F-N tunneling is also observed at LRS because of the oxygen-rich layer formed at the WO_x/W TE interface, which is reported here for the first time. The E_c values of LRS for the positive region were 2.7, 2.7, and 3.7 MV cm^{-1} and those values before reset were 2.7, 3.5, and 4 MV cm^{-1} for the S1, S2, and S3 devices, respectively. This confirmed that the transport mechanism of both LRS and HRS at the high field regions was dominated by F-N tunneling. A minimum E_c value was found to be 2.7 MV cm^{-1} from all the devices, which was also higher than the reported value of

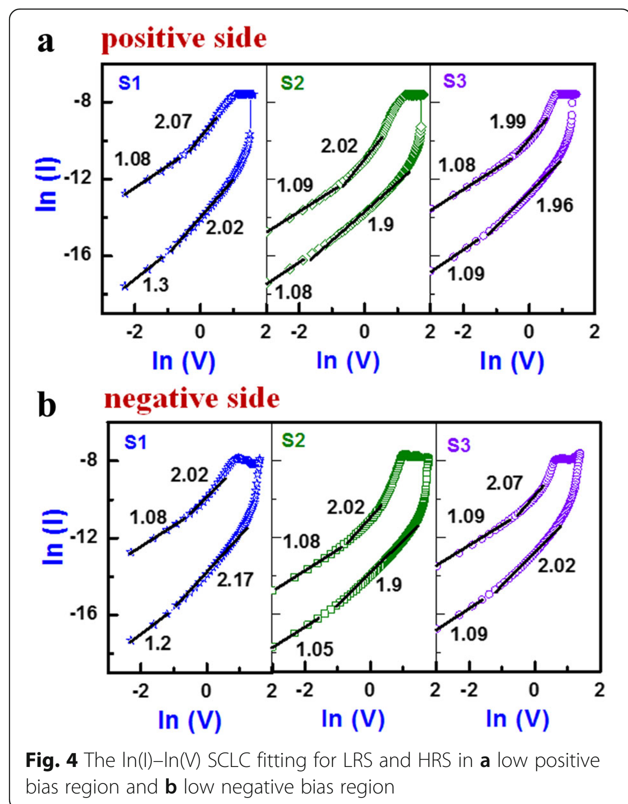

Fig. 4 The ln(I)–ln(V) SCLC fitting for LRS and HRS in **a** low positive bias region and **b** low negative bias region

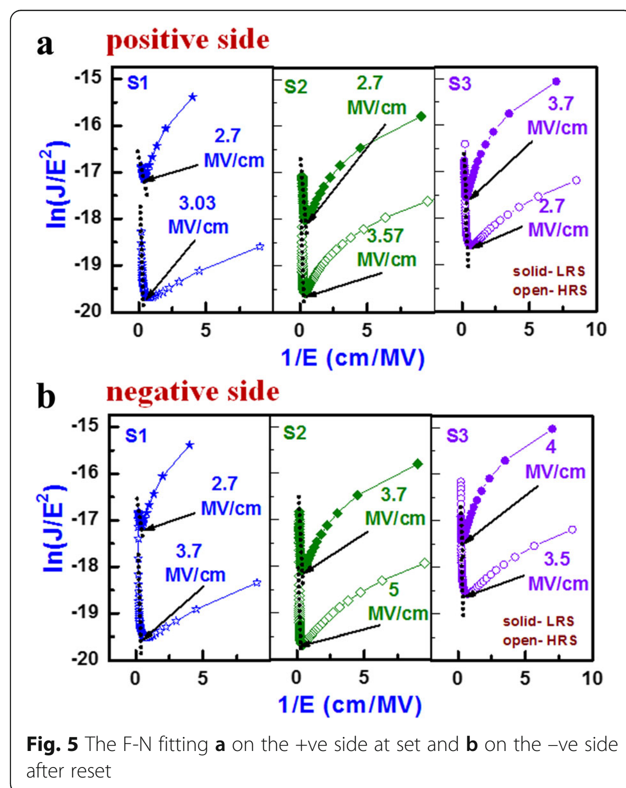

Fig. 5 The F-N fitting **a** on the +ve side at set and **b** on the −ve side after reset

2.6 MV cm^{-1} [33]. The slope of the F-N fitting curve (Fig. 5) and the value of Φ_B can be calculated by using the equation below:

$$\phi_B = \left(\frac{3h}{8\pi}\right)^{2/3} \frac{S^{2/3}}{(2qm^*)^{1/3}} \tag{3}$$

where S is the slope of the fitted line (black dotted lines). The Φ_B values at HRS for the +ve and –ve sides were 0.25/0.56, 0.31/1.03, and 0.28/0.63 eV, while those values at LRS were 0.11/0.10, 0.21/0.28, and 0.25/0.29 eV for the S1, S2, and S3 devices, respectively. All devices showed lower Φ_B in the positive bias region than the negative bias region owing to a higher work function of oxidized W (or WO_x) than the pure W metal (4.91 eV [34] vs. 4.6 eV [19]). The barrier height (Φ_B) values of electrons in HRS for the S2 devices were higher than those of the S1 and S3 devices. This is because of the annealing out of defects from the switching layer at 400 °C. At an annealing temperature of 500 °C, both Φ_B values for the S3 devices were the lower either because of N_2 incorporated into the WO_x layer or the reduction of oxygen and inter-diffusion of W into the WO_3 layer [35, 36], which can also help lower the operation voltage to ±4 V (Fig. 3). The S3 devices had the benefit of a higher non-linearity factor (η), which will help reduce the sneak paths for crossbar array applications [24]. The η is defined as $\eta = (I \text{ at } V_r)/(I \text{ at } 1/2\ V_r)$. The values of η for the S1, S2, and S3 devices were found to be 5.2, 8.6, and 8.8, respectively. Therefore, we can define the −1 V to 1 V region as the unselected region and the higher voltage region as the selected region, as shown in Fig. 3. This non-linearity resulted from the presence of the WO_3/WO_x bilayer concept in the W/WO_3/WO_x/W simple structure. In addition, the S3 devices showed stable data retention of >10^3 s at a high read voltage of 0.5 V (not shown here). However, CF formation/rupture into the WO_3/WO_x bilayer needs to be explored further, which is discussed below.

The oxygen ion migration under external bias, oxygen-rich layer formation at the WO_x/W TE interface during set, and larger dissolution gap during reset show the resistive switching characteristics. The transport characteristics are controlled by SCLC at the low bias region and F-N tunneling at higher bias regions for all the devices. Due to oxygen-rich layer formation at LRS, the F-N tunneling is observed, and after reset at the maximum value of negative voltage (−5, −6, and −4 V for the S1, S2, and S3 devices, respectively), the electrons had enough energy to F-N tunnel through the dissolution gap. By using Eqs. (1) and (2) of SCLC and F-N tunneling and using above parameters, the I-V characteristics except reset regions were simulated using MATLAB as a simulation tool. Well-fitted I-V with experimental curve for all devices is shown in Fig. 7a. The input value of ε_r was considered as 5 [37]. The μ value through the WO_3 layer was considered approximately 10^{-2} cm^2 V^{-1} s^{-1}, which is close to the reported value of 5×10^{-2} cm^2 V^{-1} s^{-1} [38]. The Φ_B values obtained from Eq. (2) were considered as those were. The value of effective mass was taken as $0.7 \times m_0$, which is close to the reported value (in the range of $0.7 \times m_0$ to $1.2 \times m_0$ [39]). A similar conduction mechanism was also reported by Kim et al. [40] and Ban and Kim [41] for different structures with switching materials. The reset regions of the S1, S2, and S3 devices were −2.5 to −5 V, −2.8 to −6 V, and −2.1 to −4 V, respectively (i.e., red symbols in Fig. 3). The I-V curves of reset regions were simulated by MATLAB using drift diffusion, current continuity, and Joule heat equations [31]. The oxygen-vacancy flux can be written as the sum of diffusion flux (J_D) and drift flux (J_d). So total current (J_{total}) is equal to:

$J_D + J_d = -D\nabla n_D + \nu n_D$, which is evaluated by:

$$\frac{\partial n_D}{\partial t} = \nabla.(D\nabla n_D - \nu n_D) \tag{4}$$

$$\nabla\sigma\nabla\psi = 0 \tag{5}$$

$$-\nabla k_{th}\nabla T = \sigma\,|\nabla\psi|^2 \tag{6}$$

where n_D is the V_0 concentration; t is the time; D [$=0.5a^2 f \exp(-U_A/k_BT)$] is the diffusivity; ν [$af\exp(-U_A/k_BT)\sinh(qaE/k_BT)$] is the drift velocity of oxygen vacancy; f is the attempt frequency (10^{13} Hz [42]); U_A is the activation potential of 1 eV, which is similar to the reported values (~1 eV [43]); and a is the hopping distance of 0.5 nm, which is similar to our previous reported value (0.56 nm [44]). At zero bias condition, the value of U_A was high. As the voltage was increased, the value of U_A became lower. The electrical conductivity (σ) is given by Arrhenius equation: $\sigma = \sigma_0 \exp(-E_{AC}/k_BT)$, where σ_0 is the pre-exponent constant and E_{AC} is the activation energy. The E_{AC} value changes from 0.01 to 0.03 eV, and it is decreasing with increasing value of oxygen-vacancy density (n_D), which is similar to the reported value of 0.06 eV [45]. Both the values of σ_0 ($WO_3 = 1.5 \times 10^2$ Ω^{-1} m^{-1} [46]; $WO_x = 7 \times 10^2$ Ω^{-1} m^{-1} [47]) and k_{th} (WO_3 = 0.2 Wm^{-1} K^{-1}; W = 173 Wm^{-1} K^{-1} [19]) varied linearly with the conductivity of WO_3 to W, and ψ was the potential. The value was taken to best fit with the experimental curve. Now we solved Eqs. (4)–(6) simultaneously with the help of MATLAB to obtain the profiles of n_D and T with different negative voltages. Consequently, I-V reset curves were obtained. The experimental and simulated I-Vs were given in Fig. 6a. The simulated I-V curves matched quite well with the experimental data. From this simulation, the thickness of the WO_3 layer was determined to be 4 nm for all structures but the thicknesses of the oxygen-rich WO_x/W TE interface under set

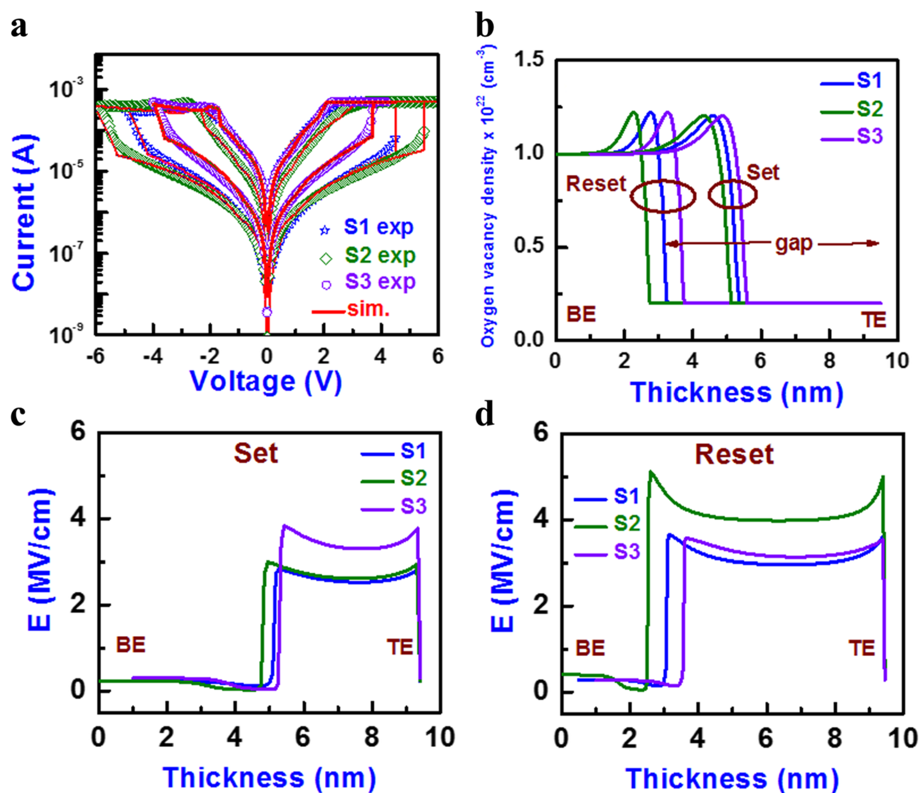

Fig. 6 a Experimental and simulated I-V in the log scale for the S1, S2, and S3 devices. **b** Oxygen-vacancy density (n_D) profiles show a different gap in the set and reset. Corresponding electric field distribution along the CF after **c** set and **d** reset

were determined to be 4, 4.5, and 3.5 nm for the S1, S2 and S3 devices, respectively. These thicknesses were also used to calculate E in Fig. 5a, b. The cylindrical CF diameter was approximately 34 nm, which is useful for nanoscale non-volatile crossbar array applications. Similar CF diameter of 10–30 nm in a Pt/NiO/Pt structure at a CC of 1 mA was reported by Yun et al. [48]. Yao et al. [49] reported a <1-nm filament diameter in a Au/α-C/SiO_x/α-C/Au structure with operation current of ~50 μA. Song et al. [50] reported about a 70-nm filament diameter in a Pt/TiO_2/Pt structure with a CC of 10 mA. Waser and Aono [51] reported an ~12-μm-diameter filament in a Cr-doped $SrTiO_3$ single crystal cell with 5-mA current. Celano et al. [13] reported about a 28-nm CF diameter using a Cu/Al_2O_3/TiN structure at a CC of 10 μA. Yazdanparast et al. [52] reported the 70-nm CF diameter using a Au/Cu_2O_3/Au structure at a CC of 10 mA. According to our previous report [3], the CF diameter is approximately 70 nm in a Cu/GeO_x/W structure at a CC of >1 mA. A larger diameter of 2 μm using a Pt/CuO/Pt structure was reported by Yasuhara et al. [53]. In addition, the variation of oxygen-vacancy density profiles (n_D) with thickness for both the set and reset for all devices are given in Fig. 6b. The value of n_D at the CF is 1×10^{22} cm^{-3}, and the CF was assumed to be broken if the concentration was below 0.5×10^{22} cm^{-3}. There is an oxygen-rich layer at the WO_x/W TE interface under set. The dissolution gap in reset for the devices showed that the device annealed at 500 °C had the smallest gap among the three devices, which was responsible for the lowest set/reset voltage and Φ_B value. Figure 6c shows the E (=$d\psi/dx$) distributions for the S1, S2, and S3 devices after set (or at LRS). After maximum reset voltages of −5, −6, and −4 V for the S1, S2, and S3 devices, respectively, the E distribution along the CF is shown in Fig. 6d. By solving Eqs. (4) and (5) for ψ and n_D, the E profiles were obtained. According to the E values at LRS along the CF and after reset (Fig. 5), this shows F-N tunneling (>2.7 MV cm^{-1}). Typical color maps of n_D for the S3 devices during set and reset are shown in Fig. 7. The oxygen-rich layer at the WO_x/W TE interface with a thickness of 3.5 nm was observed at LRS, and the dissolution gap in the CF ruptured region was approximately 7.5 nm. Basically, oxygen ion migration under external bias controls the interfacial oxygen-rich layer and dissolution gap as well as the lower and higher barrier heights which lead to LRS and HRS switching, as shown in energy band diagram under bias (Fig. 7). Comparing all devices,

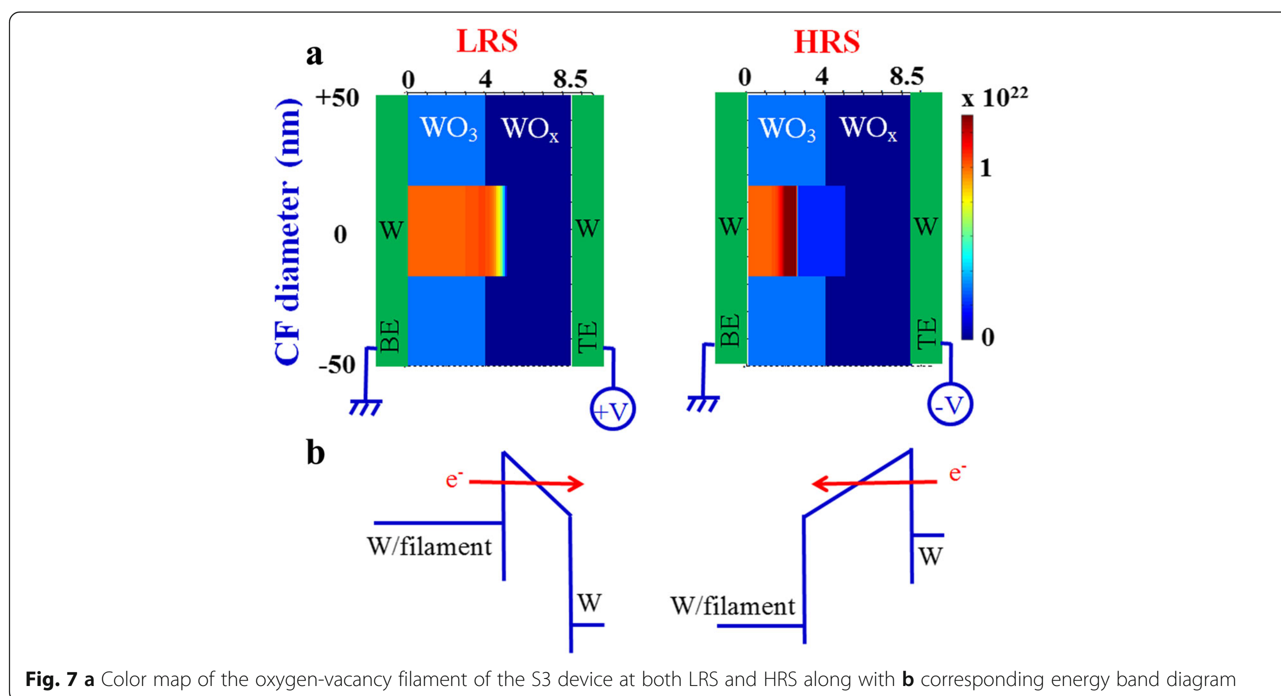

Fig. 7 a Color map of the oxygen-vacancy filament of the S3 device at both LRS and HRS along with **b** corresponding energy band diagram

the devices annealing at 500 °C showed higher non-linearity factor with lower operation voltage, and stable data retention at a high read voltage of 0.5 V, which will have the potential for nanoscale non-volatile memory applications. In addition, the I-V switching characteristics using transport and hopping conductions have been simulated using a new and simple concept, which will also help to analyze other resistive switching memory devices in future.

Conclusions

In conclusion, post-metal annealing effects on the forming-free resistive switching behavior of the $W/WO_3/WO_x/W$ structure were observed, especially F-N tunneling at LRS and after reset was observed for the first time. The WO_3/WO_x layer was confirmed by TEM and XPS. The RRAM devices annealed at 500 °C had a lower operation voltage, thinner WO_x/W TE interface, lower barrier height, and stable data retention. A simulation based on SCLC conduction in the low field, F-N tunneling in the high field for both HRS and LRS, and oxygen-vacant CF with a diameter of ~34 nm was developed for all non-linear I-V switching characteristics, which will be very useful to understand the switching mechanism for other RRAM structures and for selector-less nanoscale crossbar architectures.

Acknowledgements

This work was supported by the Ministry of Science and Technology (MOST), Taiwan, under the following contract numbers: MOST-102-2221-E-182-057-MY2 and MOST-104-2221-E-182-075, and Chang Gung Memorial Hospital (CGMH), Linkou, under contract no. CMRPD2E0091. The authors are grateful to MSSCORPS CO., LTD., Hsinchu, Taiwan, for the TEM images. The authors are also grateful to Electronics and Opto-electronics Laboratories (EOL), Industrial Technology Research Institute (ITRI), Hsinchu, Taiwan, for their partial experimental support.

Authors' Contributions

SC and SZR fabricated the RRAM devices under the instruction of SM. SS helped to analyze the SCLC and F-N tunneling. SC developed the MATLAB simulation program under the instruction of SM. HMC did the XPS characteristics and analyzed the spectra. All authors contributed to the revision of the manuscript, and they approved it for publication.

Competing Interests

The authors declare that they have no competing interests.

Author details

[1]Thin Film Nano Tech. Lab., Department of Electronic Engineering, Chang Gung University, 259 Wen-Hwa 1st Rd., Kwei-Shan, Tao-Yuan 333, Taiwan. [2]Electronic and Opto-electronic Research Laboratories (EOL), Industrial Technology Research Institute (ITRI), Hsinchu 195, Taiwan. [3]Material and Chemical Research Laboratories (MRL), Industrial Technology Research Institute (ITRI), Hsinchu 195, Taiwan.

Received: 23 June 2016 Accepted: 31 August 2016
Published online: 07 September 2016

References

1. Waser R, Dittmann R, Staikov G, Szot K (2009) Redox-based resistive switching memories—nanoionic mechanisms, prospects, and challenges. Adv Mater 21:2632
2. Prakash A, Jana D, Maikap S (2013) TaOx-based resistive switching memories: prospective and challenges. Nanoscale Res Lett 8:418
3. Jana D, Roy S, Panja R, Dutta M, Rahaman SZ, Mahapatra R, Maikap S (2015) Conductive bridging random access memory: challenges and opportunity for 3D architecture. Nanoscale Res Lett 10:188
4. Liu D, Cheng H, Zhu X, Wang G, Wang N (2013) Analog memristors based on thickening/thinning of Ag nanofilaments in amorphous manganite thin films. ACS Appl Mater Interfaces 5:11258

5. Terai M, Sakotsubo Y, Saito Y, Kotsuji S, Hada H (2009) Effect of bottom electrode of ReRAM with Ta_2O_5/TiO_2 stack on RTN and retention. In Tech. Dig.-Int. Electron Device Meet, Baltimore, pp 775
6. Kim S, Kim SJ, Kim KM, Lee SR, Chang M, Cho E, Kim YB, Kim CJ, Chung UI, Yoo IK (2013) Physical electro-thermal model of resistive switching in bi-layered resistance-change memory. Sci Rep 3:1680
7. Gao S, Zeng F, Wang M, Wang G, Song C, Pan F (2015) Tuning the switching behavior of binary oxide-based resistive memory devices by inserting an ultra-thin chemically active metal nanolayer: a case study on the Ta_2O_5–Ta system. Phys Chem Chem Phys 17:12849
8. Yu S, Chen YH, Gao B, Kang J, Philip Wong HS (2013) HfOx-based vertical resistive switching random access memory suitable for bit-cost-effective three-dimensional cross-point architecture. ACS Nano 7:2320
9. Chen YY, Goux L, Clima S, Govoreanu B, Degraeve R, Kar GS, Fantini A, Guido G, Wouters DJ, Jurczak M (2013) Endurance/retention trade-off on HfO_2/metal cap 1T1R bipolar RRAM. IEEE Trans Electron Devices 60:1114
10. Yang JJ, Pickett MD, Li X, Ohlberg DAA, Stewart DR, Williams RS (2008) Memristive switching mechanism for metal/oxide/metal nanodevices. Nat Nanotechnol 3:429
11. Bousoulas P, Giannopoulos J, Giannakopoulos K, Dimitrakis P, Tsoukalas D (2013) Memory programming of TiO_{2-x} films by conductive atomic force microscopy evidencing filamentary resistive switching. Appl Surf Sci 271:407
12. Jana D, Samanta S, Roy S, Lin YF, Maikap S (2015) Observation of resistive switching memory by reducing device size in a new Cr/CrOx/TiOx/TiN structure. Nano-Micro Lett 7(4):392
13. Celano U, Goux L, Belmonte A, Opsomer K, Franquet A, Schulze A, Detavernier C, Richard O, Bender H, Jurczak M, Vandervorst W (2014) Three-dimensional observation of the conductive filament in nanoscaled resistive memory devices. Nano Lett 14:2401
14. Lin CY, Lee DY, Wang SY, Lin CC, Tseng TY (2008) Effect of thermal treatment on resistive switching characteristics in Pt/Ti/Al_2O_3/Pt devices. Sur Coat Technol 203:628
15. Roy S, Maikap S, Sreekanth G, Dutta M, Jana D, Chen YY, Yang JR (2015) Improved resistive switching phenomena and mechanism using Cu-Al alloy in a new Cu:AlOx/TaOx/TiN structure. J Alloys Comp 637:517
16. Chien WC, Lee MH, Lee FM, Lin YY, Lung HL, Hsieh KY, Lu CY (2011) Multi-level 40 nm WO_x resistive memory with excellent reliability. In Tech. Dig.-Int. Electron Device Meet, Washington, pp 31.5.1.
17. Biju KP, Liu X, Siddik M, Kim S, Shin J, Kim I, Ignatiev A, Hwang H (2011) Resistive switching characteristics and mechanism of thermally grown WOx thin films. J Appl Phys 110:064505
18. Chang MT, Chou LJ, Chueh YL, Lee YC, Hsieh CH, Chen CD, Lan YW, Chen LJ (2007) Nitrogen-doped tungsten oxide nanowires: low-temperature synthesis on Si, and electrical, optical, and field-emission properties. Small 3:658
19. R. C. Weast (ed.) (1984) CRC Handbook of Chemistry and Physics, 64 ed., CRC Press, Taylor and Francis Group, Newyork
20. Mahapatra R, Maji S, Horsfall AB, Wright NG (2015) Temperature impact on switching characteristics of resistive memory devices with HfOx/TiOx/HfOx stack dielectric. Microelectron Eng 138:118
21. Sawa A (2008) Resistive switching in transition metal oxides. Mater Today 11:28
22. Chang KC, Tsai TM, Chang TC, Chen KH, Zhang R, Wang ZY, Chen JH, Young TF, Chen MC, Chu TJ, Huang SY, Syu YE, Bao DH, Sze SM (2014) Dual ion effect of the lithium silicate resistance random access memory. IEEE Electron Device Lett 35:530
23. Liu D, Wang N, Wang G, Shao Z, Zhu X, Zhang C, Cheng H (2013) Programmable metallization cells based on amorphous $La_{0.79}Sr_{0.21}MnO_3$ thin films for memory applications. J Alloys Comp 580:384
24. Linn E, Rosezin R, Kugeler C, Waser R (2010) Complementary resistive switches for passive nanocrossbar memories. Nat Mater 9:403
25. Mandapati R, Borkar AS, Srinivasan VSS, Bafna P, Karkare P, Lodha S, Ganguly U (2013) The impact of n-p-n selector-based bipolar RRAM cross-point on array performance. IEEE Trans Electron Dev 60:3385
26. Ottaviano L, Rossi M, Santucci S (2005) Initial stages of WO_3 growth on silicon substrates. Thin Solid Films 490:59
27. Huo N, Yang S, Wei Z, Li J (2013) Synthesis of WO_3 nanostructures and their ultraviolet photo response properties. J Mater Chem C 1:3999
28. Mwakikunga BW, Forbes A, Sideras-Haddad E, Scriba M, Manikandan E (2010) Self assembly and properties of C:WO_3 nano-platelets and C:VO_2/V_2O_5 triangular capsules produced by laser solution photolysis. Nanoscale Res Lett 5:389
29. Kawasaki H, Matsunaga T, Guan W, Ohshima T, Yagyu Y, Suda Y (2009) Preparation of WO_3 thin films for electrochromic display by plasma process. J Plasma Fusion Res Series 8:1431
30. Prakash A, Maikap S, Banerjee W, Jana D, Lai CS (2013) Impact of electrically formed interfacial layer and improved memory characteristics of IrO_x/high-kx/W structures containing AlO_x, GdO_x, HfO_x, and TaO_x switching materials. Nanoscale Res Lett 8:379
31. Sze SM, Ng KK (2007) Physics of semiconductor devices. Wiley-Interscience, New York
32. Fowler RH, Nordheim L (1928) Electron emission in intense electric field. Proc Royal Soc A 119:173
33. Chiu FC (2006) Interface characterization and carrier transportation in metal/HfO_2/silicon structure. J Appl Phys 100:114102
34. Subrahmanyam A, Karuppasamy A, Kumar CS (2006) Oxygen-sputtered tungsten oxide thin films for enhanced electrochromicproperties. Electrochem Solid-State Lett 9:H111
35. Khanna R, Pearton SJ, Ren F, Kravchenko I (2005) CrB_2 Schottky barrier contacts on n-GaN. J Electrochem Soc 152:G804
36. Reddy YM, Nagaraj MK, Naik SS, Reddy VR (2012) Annealing effects on electrical properties and interfacial reactions of Ni/Cu Schottky rectifiers on n-type InP. J Mod Phys 3:538
37. DeVries MJ, Trimble C, Tiwald TE, Thompson DW, Woollam JA, Hale JS (1999) Optical constants of crystalline WO_3 deposited by magnetron sputtering. J Vac Sci Tech A 17:2906
38. Meng X, Quenneville F, Venne F, Mauro E, Isık D, Barbosa M, Drolet Y, Natile MM, Rochefort D, Soavi F, Santato C (2015) Electrolyte-gated WO_3 transistors: electrochemistry, structure, and device performance. J Phy Chem C 119:21732
39. Crowder BL, Sienko MJ (1963) Some solid-state studies of tungsten trioxide and their significance to tungsten bronze theory. J Chem Phys 38:1576
40. Kim A, Song K, Kim Y, Moon J (2011) All solution-processed, fully transparent resistive memory devices. ACS Appl Mater Interfaces 3:4525
41. Ban S, Kim O (2014) Improvement of switching uniformity in HfO_x-based resistive random access memory with a titanium film and effects of titanium on resistive switching behaviors. Jpn J Appl Phys 53:06JE15
42. Stoneham AM (1989) Ionic Solids at High Temperatures, World Scientific Publishing Co. Pvt., Ltd., Singapore
43. Iddir H, Ogut S, Zapol P, Browning ND (2007) Diffusion mechanisms of native point defects in rutile TiO_2:Ab-initiototal energy calculations. Phys Rev B 75:073203
44. Jana D, Samanta S, Maikap S, Cheng HM (2016) Evolution of complementary resistive switching characteristics using $IrO_x/GdO_x/Al_2O_3$/TiN structure. Appl Phys Lett 108:011605
45. Wang H, Lindgren T, He J, Hagfeldt A, Lindquist SE (2000) Photolelectrochemistry of nanostructured WO_3 thin film electrodes for water oxidation: mechanism of electron transport. J Phys Chem B 104:5686
46. Yoon S, Jo C, Noh SY, Lee CW, Song JH, Lee J (2011) Development of a high-performance anode for lithium ion batteries using novel ordered mesoporous tungsten oxide materials with high electrical conductivity. Phys Chem Chem Phys 13:11060
47. Georg A, Graf W, Wittwer V (1998) Comparison of electrical conductivity and optical properties of substoichiometrically and electrochemically coloured WOx films of different crystallinity. Sol Energy Mater Sol Cells 51:353
48. Yun JB, Kim S, Seo S, Lee MJ, Kim DC, Ahn SE, Park Y, Kim J, Shin H (2007) Random and localized resistive switching observation in Pt/NiO/Pt. Phys Stat Sol (RRL) 1:280
49. Yao J, Zhong L, Natelson D, Tour JM (2012) In situ imaging of the conducting filament in a silicon oxide resistive switch. Sci Rep 2:242
50. Song SJ, Seok JY, Yoon JH, Kim KM, Kim GH, Lee MH, Hwang CS (2013) Real-time identification of the evolution of conducting nano-filaments in TiO_2 thin film ReRAM. Sci Rep 3:3443
51. Waser R, Aono M (2007) Nanoionics-based resistive switching memories. Mat Mater 6:833
52. Yazdanparast S, Koza JA, Switzer JA (2015) Copper nanofilament formation during unipolar resistance switching of electrodeposited cuprous oxide. Chem Mater 27:5974
53. Yasuhara R, Fujiwara K, Horiba K, Kumigashira H, Kotsugi M, Oshima M, Takagi H (2009) Inhomogeneous chemical states in resistance-switching devices with a planar-type Pt/CuO/Pt structure. Appl Phys Lett 95:012110